communications biology

A Nature Portfolio journal

Article

https://doi.org/10.1038/s42003-025-08981-1

Microstructural maturation of the adult mouse brain

Check for updates

Naila Rahman [1,2,5], Jake Hamilton [1,2,5], Kathy Xu[3,4], Arthur Brown[3,4] & Corey A. Baron [1,2]

While lifespan studies have consistently shown changes in diffusion MRI (dMRI) metrics indicating gradual microstructural remodeling until middle age, the cellular sources remain unclear due to the lack of microstructural specificity of traditional dMRI measurements. To provide insight into the biophysical mechanisms of dMRI changes during aging, we employ advanced techniques with improved microstructural specificity to study healthy mouse brain maturation from 3-8 months of age. Agreeing with past studies, fractional anisotropy, diffusional kurtosis and myelin-specific MRI metrics increased with age. Our main finding is that kurtosis increases were driven by increases in its sub-component of "isotropic kurtosis" (sensitive to variance of compartmental mean diffusivities), while the remaining sub-component of "anisotropic kurtosis" (sensitive to microstructural anisotropy) remained stable. These observations were accompanied by increases in myelin content and oligodendrocyte density. Our findings suggest that diffusional kurtosis increases during adult mouse brain maturation are not driven by changes in anisotropic structures like axons, but by overall heterogeneity increases that are due, at least in part, to changing oligodendrocyte populations. This work gives further insight into microstructural changes occurring during brain maturation and new insight into the biological underpinnings of dMRI contrast.

Characterizing the trajectories of neurological aging is essential for differentiating normal cognitive development and decline from pathological processes. Magnetic resonance imaging (MRI) offers a powerful, non-invasive tool for tracking structural and functional changes across the lifespan. Several cross-sectional MRI studies have been conducted over the lifespan, with most involving large multi-center datasets[1–6]. Lifespan patterns of quantitative and volumetric analyses have been widely reported to follow U-shaped or inverted U-shaped trajectories peaking ~30–40 years of age, depending on brain region, signifying that brain maturation continues until middle age, followed by degeneration at older ages. Diffusion MRI (dMRI) has been the most employed approach for these studies, as it can provide insight into cellular changes that may be occurring non-invasively[7]. Mean diffusivity (MD) follows a U-shaped trajectory in both white and gray matter, which suggests more diffusion restriction from cellular components during maturation and less during senescence. In white matter, fractional anisotropy (FA) follows an inverted U, suggesting increased alignment and/or density of axons or other fibers until middle age, which reverse in the elderly. While these results give important information on the timelines of maturation and senescence, the cellular interpretations are non-specific. Improved microstructural specificity can be obtained by acquiring additional images with a broader range of diffusion weighting parameters[8]. Diffusional kurtosis uses additional images with stronger diffusion weighting to provide information about the heterogeneity of diffusion characteristics of cells, which can stem from both anisotropic cell shape and heterogeneity in cell sizes[9,10]. This parameter shows an inverted U-shape with age, signifying tissue complexity reaches a maximum in middle age[4–6]. While Kamiya et al.[11] found the decrease in diffusional kurtosis at older ages in humans is driven by a reduction in anisotropic structures, the cellular sources responsible for its increases during maturation remain to be elucidated.

To help answer this question, we may turn to animal models as the molecular mechanisms of aging in mice are similar to those in humans[12] and they allow for longitudinal investigation due to accelerated aging processes and the ability to perform histopathological assessment. Rodent models, in particular, play an essential role in the study of disease/injury mechanisms and the development of disease-modifying therapies, with nearly 60% of studies in the life sciences using mouse models[13]. Hammelrath et al.[14] and Mengler et al.[15] demonstrated that brain maturation continues past 3 months of age in rodents using T2-weighted MRI combined with FA and

[1]Centre for Functional and Metabolic Mapping (CFMM), Robarts Research Institute, Western University, London, ON, Canada. [2]Department of Medical Biophysics, Schulich School of Medicine and Dentistry, Western University, London, ON, Canada. [3]Translational Neuroscience Group, Robarts Research Institute, Schulich School of Medicine and Dentistry, Western University, London, ON, Canada. [4]Department of Anatomy and Cell Biology, Western University, London, ON, Canada. [5]These authors contributed equally: Naila Rahman, Jake Hamilton. e-mail: corey.baron@uwo.ca

diffusivity measures from dMRI, which was linked to ongoing myelination via histology. Indeed, increases in myelination have been shown to continue well into middle age in humans and mice using myelin-specific MRI[16–18]. However, myelin water is only indirectly probed by dMRI since its short T_2 relaxation renders it invisible at the long echo times used[19]. Diffusional kurtosis has also been investigated in rats, where similar to human studies, increases in brain tissue complexity during early adult brain maturation are implicated[20,21]. Despite a recent study showing diffusional kurtosis showed excellent spatial correlation with myelin content in even gray matter[22], the mechanism for how myelination affects dMRI contrast is unclear. These past studies suggest diffusional kurtosis changes during brain maturation are related to fiber ultrastructural changes, such as axon content increases and/or myelination in white matter and dendritic architectural modifications in gray matter. Therefore, we hypothesize that increases in kurtosis during maturation will be driven by anisotropic sources of kurtosis.

In this work, we aim to gain more insight into microstructural changes that are occurring during healthy adult mouse brain maturation in the first 8 months of life using two state-of-the-art dMRI acquisitions that manipulate diffusion weighting to improve microstructural specificity beyond that previously achieved in investigations into brain maturation: "tensor-valued" and "oscillating gradient spin-echo (OGSE)" dMRI. We complement these dMRI acquisitions with "magnetization transfer saturation (MTsat)" MRI, which is a marker sensitive to myelin[23,24]. We chose to focus on 3–8 months of age, given that the upper end of the transition from maturation to senescence implicated in human studies corresponds to ~10 months of age in mice[25]. All the MRI data has been made openly available[26]. To shed light on the microstructural changes underlying these MRI measurements, we also investigate differences in histological measures of glial cells and myelin between mice aged 3 and 8 months. Our main finding is that contrary to our hypothesis, increases in diffusional kurtosis during maturation are nearly fully attributed to changes in the variance of compartmental MD (e.g., cell soma and/or the volume of extracellular space) but not changes in microstructural anisotropy. These findings, paired with concomitant increases in myelin content (measured by MTsat and histology), suggest that anisotropic kurtosis (see Theory) is insensitive to ongoing myelination during brain maturation. These observations coincided with increasing numbers of oligodendrocytes, which suggests that glial cells, which have been traditionally ignored in dMRI microstructural models and interpretation of dMRI changes in disease/injury, may have an appreciable contribution to dMRI contrast.

Theory

Tensor-valued dMRI[27–29] allows decomposition of the diffusional kurtosis into two sub-components with different microstructural underpinnings:

$$K_{total} = K_{iso} + K_{aniso} \quad (1)$$

where K_{iso} (isotropic kurtosis) is a measure of the variance in MD across all cells and extracellular space in the voxel (i.e., variance in MD across all compartments), which can be related to variance in cell size or type, and K_{aniso} (anisotropic kurtosis) is a measure of microstructural anisotropy (e.g., voxels with many axons have high K_{aniso})[9]. While K_{aniso} has similarity to FA, in contrast to FA it is not affected by the directional coherence of fibers, making it an effective index of total fiber volume even in gray matter. A related dMRI metric is microscopic fractional anisotropy (μFA), which has a monotonic relationship with K_{aniso}. Like FA it is normalized to lie within 0 and 1, but it is not confounded by orientation dispersion[30]:

$$\mu FA = \sqrt{\frac{3}{2}}\left(1 + \frac{6}{5Kaniso}\right)^{-1/2} \quad (2)$$

OGSE dMRI[31] measures how diffusivity varies with respect to frequency:

$$MD_f = MD_0 + \Lambda f^{0.5} \quad (3)$$

where Λ is the "diffusion dispersion rate[32,33]. OGSE dMRI probes diffusion time dependence in the frequency domain, where shorter diffusion times (higher frequencies) reduce the time that molecules probe their microstructural surroundings. The diffusion dispersion is therefore a measure of how diffusivity varies across spatial scales and is sensitive to cell size and structural variations along axons (e.g., axon beading)[34–36]. Supplementary Fig. 1 demonstrates that fitting diffusion dispersion with Eq. (3) provides a good fit for our data in a representative mouse at baseline, which was verified in other subjects.

Results

Representative MRI maps

Figure 1 shows representative maps for one mouse at 3 months of age. K_{aniso} shows enhanced white matter contrast compared to K_{total}, as expected, and K_{iso} is relatively consistent throughout the brain. Λ shows selective enhancement of distinct regions in the brain with densely packed neurons, such as the dentate gyrus (part of the hippocampal formation).

MRI metrics over time

From model selection testing using the corrected Akaike Information Criterion (AICc), a linear fit was the preferred model over quadratic in 18/21 tests, with quadratic fits being the preferred model for FA in white matter (WM) (ΔAICc = 0.017) and the hippocampus (HC) (ΔAICc = 0.692) and MTsat in WM (ΔAICc = 1.218) (Supplementary Table 1). Overall, linear trends were expected given the age range of 3–8 months is during only the first half of U-shaped trajectories that peak near middle age[20].

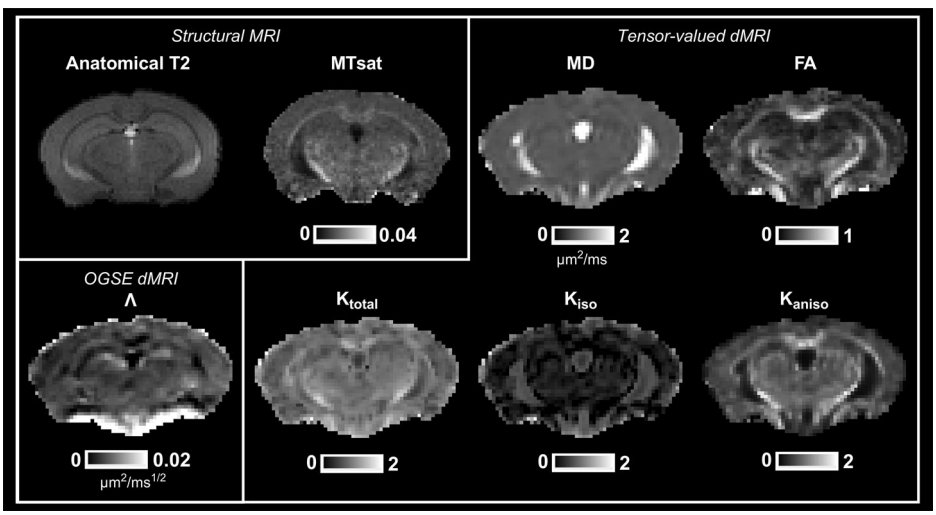

Fig. 1 | Representative axial parameter maps from one mouse at 3 months of age. Structural maps include T2-weighted and MTsat (magnetization transfer saturation). Maps from the OGSE dMRI protocol include Λ (the diffusion dispersion rate). Maps from the tensor-valued dMRI protocol include MD (mean diffusivity), FA (fractional anisotropy), K_{total} (total kurtosis), K_{iso} (isotropic kurtosis), K_{aniso} (anisotropic kurtosis).

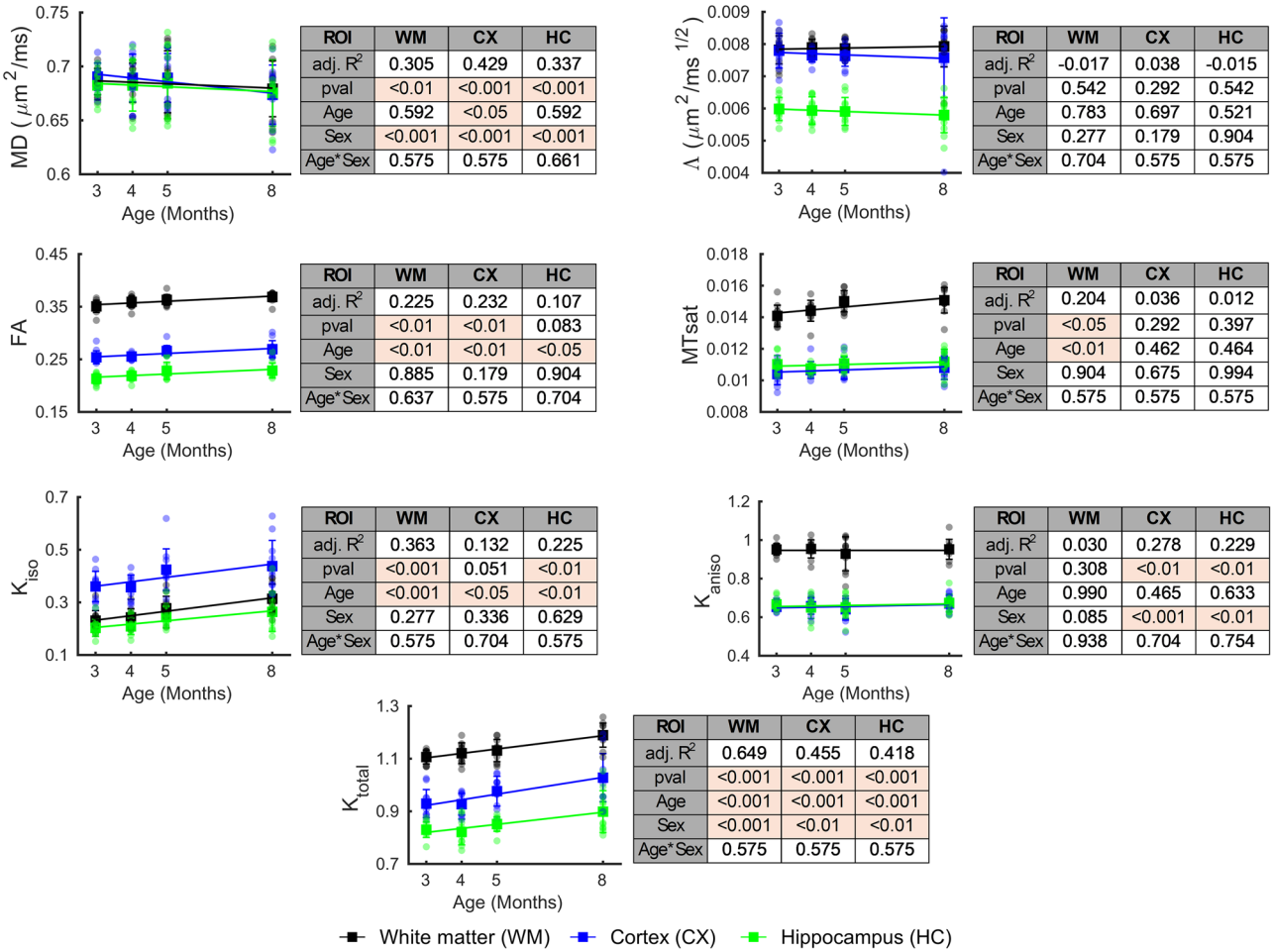

ROI	WM	CX	HC
adj. R^2	0.305	0.429	0.337
pval	<0.01	<0.001	<0.001
Age	0.592	<0.05	0.592
Sex	<0.001	<0.001	<0.001
Age*Sex	0.575	0.575	0.661

ROI	WM	CX	HC
adj. R^2	-0.017	0.038	-0.015
pval	0.542	0.292	0.542
Age	0.783	0.697	0.521
Sex	0.277	0.179	0.904
Age*Sex	0.704	0.575	0.575

ROI	WM	CX	HC
adj. R^2	0.225	0.232	0.107
pval	<0.01	<0.01	0.083
Age	<0.01	<0.01	<0.05
Sex	0.885	0.179	0.904
Age*Sex	0.637	0.575	0.704

ROI	WM	CX	HC
adj. R^2	0.204	0.036	0.012
pval	<0.05	0.292	0.397
Age	<0.01	0.462	0.464
Sex	0.904	0.675	0.994
Age*Sex	0.575	0.575	0.575

ROI	WM	CX	HC
adj. R^2	0.363	0.132	0.225
pval	<0.001	0.051	<0.01
Age	<0.001	<0.05	<0.01
Sex	0.277	0.336	0.629
Age*Sex	0.575	0.704	0.575

ROI	WM	CX	HC
adj. R^2	0.030	0.278	0.229
pval	0.308	<0.01	<0.01
Age	0.990	0.465	0.633
Sex	0.085	<0.001	<0.01
Age*Sex	0.938	0.704	0.754

ROI	WM	CX	HC
adj. R^2	0.649	0.455	0.418
pval	<0.001	<0.001	<0.001
Age	<0.001	<0.001	<0.001
Sex	<0.001	<0.01	<0.01
Age*Sex	0.575	0.575	0.575

Fig. 2 | Microstructural MRI metric changes from 3 to 8 months of age across 3 regions of interest. Results of multiple linear regression reported in table next to the corresponding graph, reporting the adjusted R^2 and p-value for the model fit, along with the p-values for effects of age, sex, and age*sex interaction for each ROI. Data shown as mean +/- SD across $n = 11$ subjects along with individual values (circles), with the linear fit shown for each ROI (WM white matter, CX cortex, HC hippocampus).

Subsequently, we performed multiple linear regression with age, sex, and interaction effects to metric changes over time in our ROIs (Fig. 2). Statistically significant model fits were found for MD and K_{total} (all ROIs), FA (WM and cortex (CX)), MTsat (WM), K_{iso} (WM and HC), and K_{aniso} (CX and HC). K_{iso} (CX) and FA (HC) showed an insignificant model fit but significant effect of age, and upon performing simple linear regression after removing sex as a variable as it was not contributing to the global model, a significant age effect was found (K_{iso}: $F_{1,42} = 8.042$, adj. $R^2 = 0.141$, $p < 0.01$, FA: $F_{1,42} = 8.185$, adj. $R^2 = 0.143$, $p < 0.01$).

FA showed significant increases over time in all ROIs while MD showed a decrease only in the CX. K_{total} and K_{iso} show significant increases with age in all ROIs, paired with increases in MTsat, significant in WM, while K_{aniso} remained stable with age in all ROIs. Supplementary Fig. 2 shows that μFA and K_{aniso} follow similar trends over time and between regions. Λ did not show any significant changes with age.

Significant effects of sex were found for MD and K_{total} in all ROIs and K_{aniso} in the CX and HC, while no significant sex-by-age interactions were found. We separated data by sex for all metrics to further examine these sex differences (Supplementary Fig. 3). Females show significantly higher MD compared to males in all ROIs, while males and females show remarkably similar FA values. Females show lower K_{total} and K_{aniso} compared to males.

MRI changes with time in smaller regions

To examine whether MRI changes in the larger ROIs are consistent across different smaller regions, we examined metric changes in individual WM (corpus callosum (CC), fornix (Fnx), internal capsule (IC)) and gray matter (cerebellum (Cb), hypothalamus (Hyp), thalamus (Thl)) ROIs (Fig. 3). Statistically significant model fits were found for K_{total} in all ROIs, MD (CC, IC, Cb, Hyp, Thl), MTsat (CC, Fnx and IC), and K_{iso} (IC and Thl). FA (CC), K_{iso} (Fnx), and K_{aniso} (Fnx, Cb and Thl) showed insignificant model fits but significant effects of age or sex, upon performing simple linear regression after removing the variable not contributing to the global model, a significant effect was found for all (FA (CC) – Age ($p < 0.01$), K_{iso} (Fnx) – Sex ($p < 0.01$), K_{aniso} (Fnx) – Age ($p < 0.01$), K_{aniso} (Cb) – Sex ($p < 0.05$), and K_{aniso} (Thl) – Sex ($p < 0.01$)).

A significant increase in FA with age was detected in the CC, while MD showed a significant decrease in the IC. MTsat showed significant increases with age in all WM regions (CC, Fnx, and IC), while Λ showed no significant age effect. Significant increases in K_{total} were found in all ROIs, paired with increases in K_{iso} in the IC and Thl and K_{aniso} in the Fnx. Full statistical findings are included in Supplementary Table 2.

Significant effects of sex were found for MD in most regions (CC, IC, Cb, Hyp, and Thl), K_{total} in all ROIs, K_{iso} in the Fnx, and K_{aniso} in the Cb and Thl, with no significant sex-by-age interactions found. Supplementary Fig. 4 shows these metrics separated by sex. Similar to the larger ROIs, females show higher MD and lower kurtosis.

Histology

Given the surprising finding of increases in diffusional kurtosis during maturation being driven by K_{iso}, we performed quantitative histology for

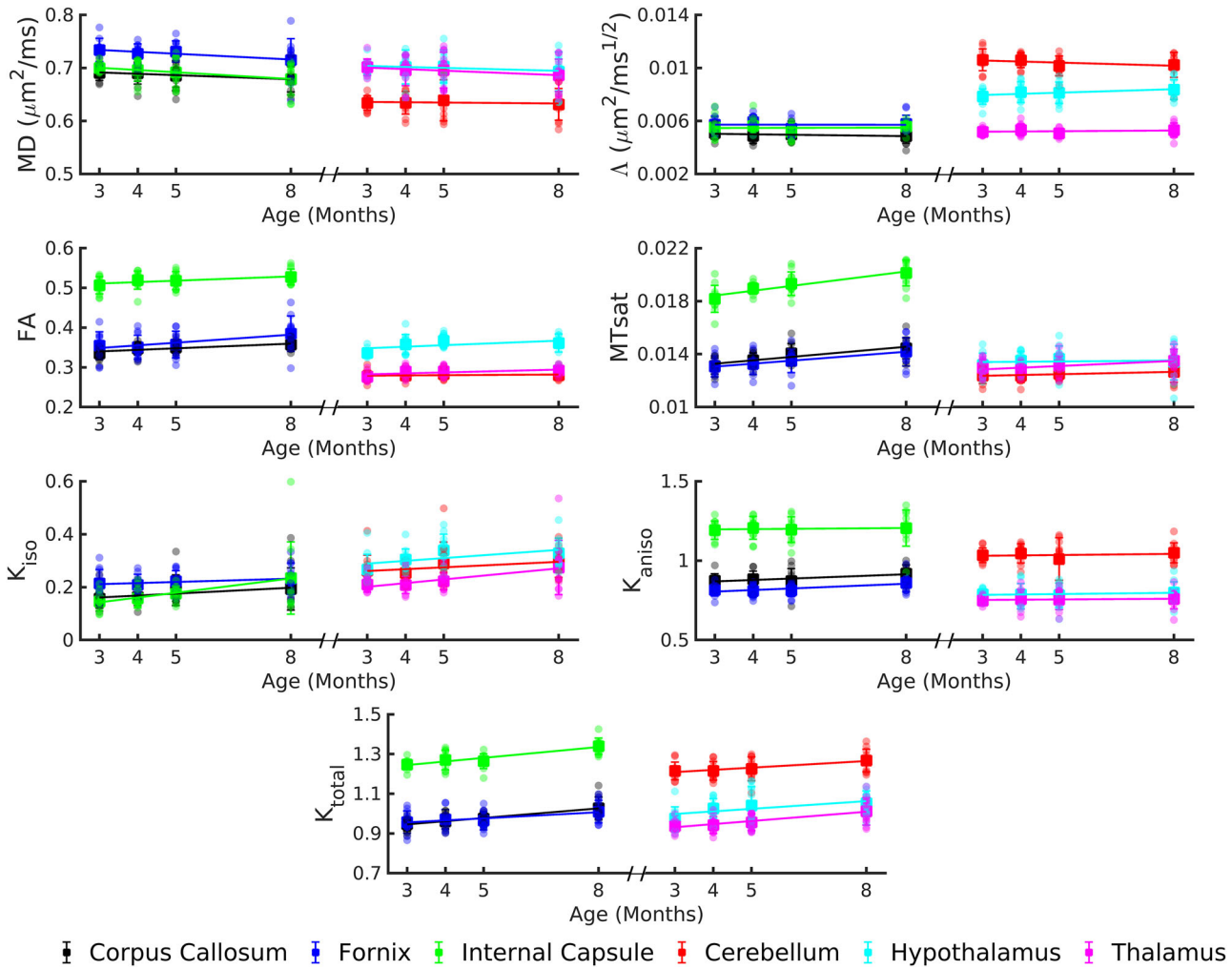

Fig. 3 | Microstructural MRI metric changes from 3-8 months of age across 6 regions of interest, including 3 white matter (corpus callosum, internal capsule, fornix system) and 3 gray matter regions (cerebellum, hypothalamus, thalamus). Data shown as mean ±SD across $n = 11$ subjects along with individual values (circles), with the linear fit shown for each ROI.

myelin and glial cell content to identify the cellular change(s) responsible. A significant increase in oligodendrocyte and myelin content (measured by Olig2 and MBP, respectively) from 3 to 8 months of age are found in all regions examined (Fig. 4). Conversely, no differences in microglia or astrocyte content were identified with Iba-1 and GFAP, respectively (Supplementary Fig. 5).

Discussion

Here we explored healthy mouse brain maturation using tensor-valued dMRI, OGSE, dMRI, and MTsat MRI to separate sources of diffusional kurtosis, probe diffusion dispersion, and characterize myelin content, respectively. These protocols were applied longitudinally in mice between 3 and 8 months of age to better understand the contrast mechanisms of these advanced MRI metrics and how they evolve over the course of normal brain maturation. Our main finding is that contrary to our and past study hypotheses, increases in diffusional kurtosis over time were driven by isotropic kurtosis and paired with increases in myelin content and oligodendrocyte density, while anisotropic kurtosis remained stable across timepoints throughout most of the brain. Age-invariant sex differences were detected in both diffusivity and kurtosis metrics, but significant age-by-sex interactions were not. Here we summarize the key interpretations of these results, followed later with comparisons to existing literature and more detailed discussion.

Our histological findings highlight that there are two microstructurally distinct components of myelination in the maturing mouse brain: increased myelination of axons (measured with MBP) and generation of the oligodendrocytes that produce the myelin (measured with OLIG2). Myelin sensitive MRI like MTsat is primarily sensitive to the former component, because of the high lipid content of the tightly wrapped layers of myelin.

Our finding that K_{aniso} is stable over time, even though axons are becoming more myelinated, suggests that K_{aniso} is insensitive to myelination. However, we cannot exclude the possibility that competing effects may be occurring, whereby myelination increases K_{aniso} and another microstructural alteration decreases K_{aniso}. Nevertheless, the complementary microstructural specificities between myelin-sensitive MRI like MTsat and K_{aniso} implicated by this work may be useful for the study of demyelinating conditions.

Our finding that increases in K_{total} during brain maturation are driven by K_{iso} suggests that diffusional kurtosis may be sensitive to myelination only indirectly through: (1) proliferation of oligodendrocytes, and (2) replacement of extracellular space (contributor to K_{iso}) with myelin (invisible to dMRI). The relative contributions of these two potential sources of K_{iso} change and other potential microstructural sources for K_{iso} increases over time cannot be easily determined from this work.

The tensor-valued dMRI results also reveal that the differences in K_{total} between white and gray matter (governed by microstructural anisotropy,

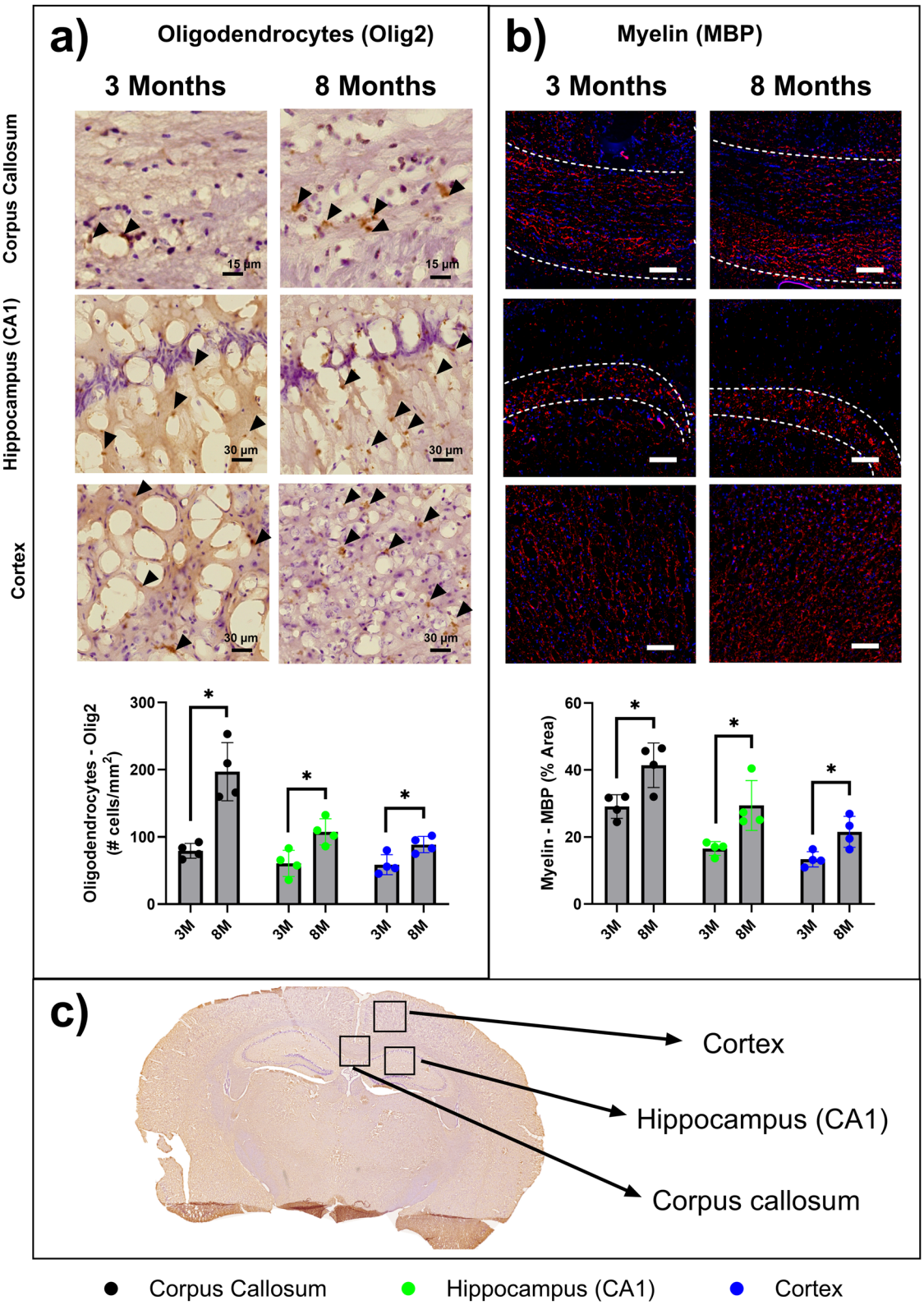

Fig. 4 | Quantitative histology at 3 and 8 months in the corpus callosum, hippocampus (CA1 subfield), and cortex. a oligodendrocytes (brown cells, some of which are highlighted by black triangles). Scale bars represent 15 µm (corpus callosum) and 30 µm (hippocampus and cortex). **b** myelin (red) and DAPI (blue) to show all cells. Scale bars represent 100 µm. Myelin in the hippocampus (CA1) was quantified in the SLM (stratum lacunosum moleculare) region, as shown with white dashed lines. Plots show mean and SD across $n = 4$ subjects along with individual values (circles), $^*p < 0.05$. **c** The specific regions imaged are shown.

K_{aniso}) stems from a microstructural source distinct from the changes over time (governed by variance in compartmental diffusivities, K_{iso}). Accordingly, this finding highlights a potential pitfall in interpretation of imaging results: the conclusion that because MTsat and K_{total} have similar spatial patterns (both high in WM) they must have similar mechanisms behind changes over time, which is shown to not necessarily be the case here.

Trends observed in MD and FA are comparable to previous human and rodent studies investigating healthy brain maturation[1,3,14,15,37]. FA shows

significant increases over time in all ROIs, while MD decreases (significant in the CX), consistent with our timepoints being in the 'young' regime of U-shaped curves described for lifespan studies (Fig. 2). Hammelrath et al. reported that in most white matter ROIs, FA continuously increased in agreement with increased intensity on myelin staining, in mice studied until 6 months of age[14]. Mengler et al. found a pronounced increase in myelinated fibers, using histology, in the cortex between 3 – 6 months of age in rats[15]. They interpreted that the decrease in MD with age was likely due to myelination. The lack of consistent MD decrease across ROIs observed here may be partially due to inclusion of both males and females in our analysis, as both aforementioned studies used only male rodents and we see a trend of greater MD decrease with age in males compared to females (Supplementary Fig. 3). Additionally, the short diffusion time (9.2 ms) used to compute DTI metrics may decrease the sensitivity of MD in detecting changes in restrictions/hindrances that occur throughout maturation.

Our histological finding of increased myelin (as measured with MBP) between 3 and 8 months aligns with past studies[14,15,38,39]. Despite significant increases in MBP in all examined regions, MTsat only showed significant increase in white matter. This suggests that MTsat is less sensitive to myelin changes in gray matter regions, which has been suggested in a study of multiple sclerosis[40]. More recent techniques, such as inhomogeneous MT (ihMT) MRI increase specificity to myelin due to its direct sensitivity to the phospholipids in myelin[41], which should be utilized in future studies investigating the impact of myelination of dMRI contrast.

K_{total} shows significant increases with age in all examined ROIs, agreeing with previous DKI studies in normal brain maturation[4,20,21]. Previous literature has related K_{total} increases to myelination and dense packing of axon fibers in white matter, and more densely packed structures like cells or membranes and dendritic architectural modifications in gray matter. However, these interpretations involving fiber microstructure would be expected to coincide with increases in K_{aniso}, which was not seen here in most of the brain (with a notable exclusion being the fornix). By investigating both isotropic and anisotropic kurtosis components in this study, we observe that during normal brain maturation, changes in K_{total} are primarily driven by changes in K_{iso}. This is paired with increasing MTsat (significant in WM) and increasing histological myelin content in white matter, cortex, and hippocampus ROIs (Fig. 4), while K_{aniso} remains stable over time. This suggests myelination in the mature brain is not a main contributor to K_{aniso} or μFA, which has a monotonic relationship with K_{aniso}[29,30,42]. A recent study found that diffusional kurtosis showed excellent spatial correlation with myelin density in both white and gray matter regions[22]. Importantly, our findings suggest that it may not be myelin increasing diffusion anisotropy within or surrounding axons responsible for this correlation but rather glial cell populations and/or extracellular volume changes (reflected in K_{iso}) or variation in the density and/or caliber of axons (reflected in K_{aniso}). Although previous studies found changes in μFA with demyelination in the cuprizone demyelination model[43] and multiple sclerosis patients[44], we suspect that damage to axons and/or neuroinflammation may have influenced resultant changes in μFA and K_{iso}.

It is interesting to note that although K_{aniso} remains stable, FA shows increases over time, which may be due to fibers becoming more aligned through maturation while their density remains consistent. As fibers become more aligned, FA is expected to increase, as macroscopic water diffusion anisotropy increases, but K_{aniso} is not expected to change, as it disentangles effects of fiber orientation dispersion from microstructure[30,45]. Significant undulation has been observed in axons using microscopy[46], which would be expected to lower FA but not K_{aniso}. However, how these undulations may change during brain maturation is an open question.

The increase in K_{iso} reflects increased cell size and density heterogeneity and changes to the extracellular volume, as it indicates a heterogeneous microenvironment with compartments having a wide variation in diffusivities within a voxel[9,47]. Given our histological findings of increased oligodendrocyte (OL) content from 3 to 8 months, we suspect that the proliferation and maturation of OLs is contributing to this increased cell size/density heterogeneity. Although most OL precursor cell (OPC) proliferation, differentiation to myelinating OLs, and myelin development occur before 3 months of age, these cellular changes occur continuously throughout adulthood at lower stable rates[39,48]. A study by Tripathi et al.[49] showed increased OL content until 8 months of age and greater increases in the corpus callosum compared to other regions, agreeing with our findings in Fig. 4. Furthermore, a recent study in humans found that oligodendrocyte-specific gene expression increases in cortical regions from 0-30 years of age, relying on the assumption that expression is proportional to OL density[50]. Agreeing with past studies[51,52], we show no changes in astrocyte and microglia density between 3 and 8 months of age (as measured by GFAP and Iba-1, respectively). However, studies have found astrocytes and microglia undergo morphological changes and continuous repopulation throughout normal brain maturation[51,53] which could impact dMRI contrast. Furthermore, while Iba-1 is considered to be a marker for all microglia[54], GFAP is more strongly expressed in reactive astrocytes, which may limit our sensitivity to detect changes in the number of non-reactive astrocytes[55].

It is possible that changes in K_{iso} are reflective of these various microstructural changes in oligodendrocytes, astrocytes, and microglia to some degree. However, oligodendrocytes are the most numerous glial cells in the mouse brain, composing >50% of glial cells[56], and thus changes in OL populations are likely to have the largest impact on dMRI parameters. The effect of glial cells on dMRI contrast is being increasingly recognized, with a recent study in humans showing that increased oligodendrocyte-specific gene expression was associated with decreased dMRI-derived apparent soma radius in the cortex[50]. Furthermore, oligodendrocytes are distributed widely throughout and undergo continuous proliferation and differentiation in both WM and GM regions[39]. This supports our findings of K_{iso} increases being at least partially related to OL populations as we show K_{iso} increases in all global ROIs. However, the consistent K_{iso} changes across these regions, paired with much lower OL density in CX and HC compared to WM, suggests there may be other contributing factors to K_{iso} changes. In the CX and HC, neuron cell body morphology and density changes could also be a contributing factor to K_{iso} changes with age. It should be noted that regional variation in K_{iso} is likely to be related to more factors than just OL populations, as K_{iso} values are largest in the CX while OL density is highest in WM[39,56,57].

A potential contributing factor to our dMRI changes is changes in perivascular space (PVS). These fluid-filled channels that surround blood vessels in the brain have been suggested to have an appreciable effect on dMRI parameters[58]. A large human study showed that in both WM and the basal ganglia, PVS volume fraction increases with age[59], which would be expected to increase K_{total} due to a wider variance in compartmental diffusivities. While studies have demonstrated that the PVS is anisotropic at relatively long diffusion times available on human scanners[58], given the short diffusion times (9.2 ms) used for kurtosis computation here, this compartment may appear as isotropic and thus be reflected predominantly by K_{iso}. However, further study of how PVS changes can impact dMRI parameters is warranted.

The dMRI metric changes observed in the three global ROIs were relatively consistent with changes in smaller ROIs, with increased MTsat in WM regions, increased FA (significant in CC), increased K_{total} (significant in CC, IC, Cb, Thl), and increased K_{iso} (significant in IC and Thl) (Fig. 3 and Supplementary Table 2). However, while most other regions show stable K_{aniso} as observed in global ROIs, the fornix shows the opposing trend with a significant increase in K_{aniso}. This suggests that while increases in cell heterogeneity drives increases in K_{total} for global ROIs, increases in the fornix may be driven by increased axonal content and/or changes in axon caliber. While we try to mitigate partial volume effects by excluding voxels with high MD, the fornix is located very close to lateral ventricle which may bias dMRI metric values.

Age-invariant sex differences were seen in MD and K_{total} in all larger ROIs and K_{aniso} in CX and HC, while no differential age-dependence (age*sex interaction) was detected for any metrics/ROI (Fig. 2 and Supplementary Fig. 3), with no differences in MTsat. These findings were

consistent with sex differences found in smaller ROIs (Supplementary Table 2 and Supplementary Fig. 4). Age-invariant differences in brain microstructure have been reported[1,60–62], with males often having more diffusion restriction (lower MD) compared to females[63], which agrees with our finding of lower MD in males. While it is more difficult to interpret the differences in K_{aniso}, simulations in Zhou et al.[64] showed increasing K_{aniso} with larger intra-axonal volume fraction. The larger K_{aniso} (and K_{total}) and smaller MD in males can thus be interpreted as a larger intra-axonal volume fraction in males compared to females. This aligns with a study utilizing microstructural modeling that showed males tend to have larger measures of intra-axonal volume fraction[62], and females tend to have smaller caliber axons than males[65]. While we did not detect differential metric trajectories between sexes, we are likely underpowered to detect these differences due to our small sample size ($n = 6$ males, $n = 5$ females). The addition of more timepoints and animals is needed to fully examine these differences.

This investigation has several limitations. Firstly, we are not able to calculate microscopic or intra-compartmental diffusional kurtosis (μK), which is another source of total kurtosis and ignoring it can bias the estimate of other kurtosis sources[66,67]. μK is the weighted sum of different microscopic sources of non-Gaussian diffusion, including restricted diffusion inside compartments with complex shapes, and microstructural disorder due to the presence of microscopic hindrances to water molecules (such as membranes and axon caliber variations)[68]. Recently, μK was shown to be a primary driver of total kurtosis upon ischemia in mice[69], revealing that this component can be non-negligible.

Secondly, we only explored the brain maturation phase of the lifespan, while the senescence phase remains to be investigated. Including more timepoints after 8 months would allow for a more robust and complete picture of the mouse brain lifespan trajectory. However, the age range used in this study is a widely accepted time period for longitudinal rodent neuroimaging studies and will provide insight into healthy rodent brain maturation, helping to disentangle normal and pathological microstructural changes. Additionally, the use of newer anatomical atlases built on in vivo contrast and incorporating both sexes could be utilized for future aging studies to examine sex differences[70].

Our histological limitations include a small sample size and staining for general glial cell populations, such as oligodendrocytes. Future studies would benefit from staining for specific cell populations, such as OPCs, premyelinating OLs, and myelinating OLs, as Olig2 is expressed on both OPCs and mature OLs[71]. A more comprehensive morphological analysis could have benefited dMRI interpretation, such as examining ramification density, soma size, and others, as we only examined stained area (MBP, GFAP, Iba1) and cell density (Olig2). Additionally, we did not quantify changes in neuron levels over time as this could impact our findings of increased cell heterogeneity in gray matter regions. However, a past study quantified NeuN (marker for neurons) throughout mouse brain maturation and found no differences in almost all regions during our study timeframe[72]. Additionally, consistent K_{iso}/K_{aniso} changes across global ROIs suggest similar microstructural changes occurring throughout the brain, although our findings in gray matter regions could have been impacted by changes in neuron levels. However, testing correlation between MRI and histology was challenged due to only 8-month-old mice being matched with MRI, while the 3-month-old mice belonged to a different batch.

Given the high performance of the gradient hardware, effective diffusion times were overall low (9.2 ms diffusion time for multi-shell LTE acquisition). While not in itself a limitation, the finding of negligible sensitivity of K_{aniso} to myelination may not hold true at longer diffusion times where compartmental exchange becomes relevant[73,74].

We did not perform microstructural modeling based on the MRI measurements, opting to focus on "representations"[75]. While modeling could potentially improve the interpretation of results, there are potential pitfalls in the microstructural assumptions that are required when performing them[76] and many possible permutations to consider for this work (glial cells, axon undulations and caliber variation, packing arrangement, cell size, etc). Additionally, microstructural models, such as SANDI[77] and NEXI[74] require higher b-value acquisitions than those acquired here (2000 s/mm^2) for accurate parameter estimation. Nevertheless, we have provided all raw imaging data open access, which may be a resource for groups specialized in the development and application of microstructural models.

In conclusion, we examined the evolution of microstructural MRI metrics longitudinally during normal mouse brain maturation, to both characterize how these metrics change over time and better understand their biological underpinnings. The trends of FA, kurtosis, and myelin-specific metrics were comparable to previous rodent and human lifespan studies. However, by decomposing diffusional kurtosis into two distinct sources, we found that metrics specific to anisotropic sources of kurtosis were stable over time and kurtosis increases during brain maturation are driven by heterogeneity in compartmental diffusivities. Histology indicated that increases in oligodendrocyte populations over time may have a role in driving these trends.

Methods

All animal procedures were approved by the University of Western Ontario Animal Care Committee and were consistent with guidelines established by the Canadian Council on Animal Care. We have complied with all relevant ethical regulations for animal use. Detailed information on the data acquisition and analysis pipeline used for this study, including the dataset, is openly available[26]. Moreover, the test-retest reproducibility of the MRI metrics have been reported previously[78,79]. Therefore, we will only summarize acquisition and analysis and refer the reader to the linked papers for full detailed methods.

Subjects

Data used for this study included 12 C57Bl/6 mice (six males, six females) scanned at 3, 4, 5, and 8 months of age. As these mice were part of a larger longitudinal study, they were anaesthetized 2 days after the first scan (at 3 months of age) by intraperitoneal injection with Ketamine 80 mg/kg and Xylazine 10 mg/kg, diluted in saline. We chose to exclude 'Day 3' and 'Week 1' data from Rahman et al.[26] to avoid possible short-term effects from ketamine/xylazine anesthesia on tissue microstructure[80]. For this study, we used data from 11 mice (six males, five females), as one female mouse did not receive a scan at all timepoints.

Before scanning, anesthesia was induced by placing the animals in an induction chamber with 4% isoflurane and an oxygen flow rate of 1.5 L/min. Following induction, isoflurane was maintained during the imaging session at 1.8% with an oxygen flow rate of 1.5 L/min through a custom-built nose cone. After the last time point, the mice were euthanized. Four mice (two females and two males) were chosen randomly for histology. The mice were anesthetized with ketamine/xylazine (2:1) and then underwent transcardiac perfusion with ice-cold saline, followed by 4% paraformaldehyde in phosphate-buffer saline (PBS). Four more mice (two females and two males), aged 3 months, were acquired for histological comparison and housed in the same conditions.

Data Acquisition

MRI experiments were conducted at the Center for Functional and Metabolic Mapping (Western University) on a 9.4 T Bruker Neo small animal scanner equipped with a gradient coil insert of 1 T/m strength. During each imaging session, OGSE and tensor-valued dMRI, MTsat MRI, and anatomical data were acquired with a total scan time of 2 h and 35 min. Anatomical images were acquired using a T2-weighted TurboRARE sequence with parameters: in-plane resolution 150 × 150 μm, slice thickness 500 μm, TE/TR = 40/5000 ms, 16 averages, total scan time of 22 min. The OGSE dMRI protocol utilized a fixed gradient duration of 11 ms and included a PGSE sequence (diffusion time = 12.9 ms) and OGSE sequences with frequencies of 50, 100, 145, and 190 Hz with a single b-value shell of 800 s/mm^2 (10 directions)[81] and parameters: in-plane resolution 175 × 200 μm, slice thickness 500 μm, TE/TR = 39.2/10000 ms, five repetitions, total scan time of 45 min. Frequency tuned bipolar (FTB) waveforms were used at 50 Hz to

lower the TE of the acquisition[82]. The tensor-valued dMRI protocol utilized a fixed gradient duration of 5.5 ms and consisted of linear (LTE) (diffusion time = 9.2 ms) and spherical tensor encoding (STE) acquisitions with b-value shells of 1000 s/mm^2 (12 LTE/STE) and 2000 s/mm^2 (30 LTE/STE) with parameters: in-plane resolution 175 × 200 µm, slice thickness 500 µm, TE/TR = 26.8/10,000 ms, three repetitions, total scan time of 45 min. The MT protocol included three FLASH-3D scans and one B1 map scan to correct for local variations in flip angle. The FLASH-3D scans consisted of an MT-weighted scan, and reference T1-weighted and PD-weighted scans with parameters: in-plane resolution 150 × 150 µm, slice thickness 500 µm, 12 averages, total scan time of 43 min.

Histological examination

Eight brains (four brains aged 3 and 8 months, with equal numbers of males and females) were post-fixed overnight, placed in 20% sucrose (as a cryopreservation procedure), and embedded in optimal cutting temperature (OCT) medium. The brains were cryosectioned at 16 µm and collected serially onto Superfrost Plus slides and stored at −80 °C. For staining, cryosections were rinsed in 0.1 M PBS and blocked in 5% goat serum with 0.3% Triton X-100 for 2 h at room temperature. The sections were then incubated with primary antibodies (diluted in 5% goat serum) at 4 °C overnight.

Primary antibodies (Supplementary Table 3) included antibodies against oligodendrocyte transcriptor factor 2 (Olig2), glial fibrillary acidic protein (GFAP), ionized calcium-binding adapter molecule 1 (Iba-1), and myelin basic protein (MBP) as markers of all oligodendrocytes, astrocytes, microglia, and myelin, respectively. Immunofluorescent staining was used to visualize astrocytes, microglia, and myelin, while DAB (3,3'-diaminobenzidine) staining was used to visualize oligodendrocytes. For immunofluorescent staining, sections were blocked with 5% Goat Serum and 0.1% Triton X-100 for 2 h at room temperature, then incubated with primary antibodies (Supplementary Table 1) at 4 °C overnight. The next day, sections were incubated for 45 min with donkey anti-mouse IgG, conjugated with Alexa Fluro 488 (Invitrogen, Eugene OR, USA) and/or a donkey anti-rabbit IgG, conjugated with Alexa Fluro 594 (Invitrogen). Sections were mounted with ProLong Diamond Antifade Mountant with DAPI (Invitrogen). DAB staining, to detect Olig2, was performed using the Vectastain Elite ABC kit (Vector laboratories, Burlingame, CA). DAB is oxidized by hydrogen peroxide in a reaction catalyzed by horseradish peroxidase (HRP) to form a brown precipitate, which can be visualized by light microscopy. Sections were incubated with 0.3% hydrogen peroxidase for 45 min to quench endogenous peroxide activity. Similar to immunofluorescent staining, blocking was performed with 5% Goat Serum and 0.3% Triton X-100 for 2 h at room temperature, then sections were incubated with the primary antibody at 4 °C overnight. The next day, sections were incubated with the secondary antibody, biotinylated-anti-rabbit IgG (1:200 dilution) for 1 h, and then with ABC (Avidin Biotin Complex containing HRP) reagent for 2 h at room temperature. Finally, DAB reagents were added, and sections were mounted with Cytoseal (Thermos Scientifics).

Digital images were captured using a Leica Mica microscope and were focused on the corpus callosum (white matter), somatomotor area (cortex), and CA1 (hippocampus) to match MRI findings, as shown in Fig. 4c. To achieve high accuracy and consistency among all samples, we adapted an atlas-guided approach and used stereotactic coordinates to define the specific brain regions: corpus callosum (bregma 0 to 1 mm), CA1 (bregma -1.5 to -2.5 mm), and somatomotor area (bregma 0.5 to 1.5 mm). For quantitative analysis, in each region, three sections collected 320 µm apart were imaged to acquire an average for each mouse, similar to previous studies[83]. All images were acquired at 20x magnification. Oligodendrocyte cell counting was performed manually. MBP, GFAP, and Iba-1 immunofluorescence was quantified using Fiji software[84], after applying a threshold of approximately 60.

Data analysis

Complex-valued repetitions were combined using in-house MATLAB code which included frequency and signal drift correction[85] and phase alignment. The DESIGNER pipeline[86] was used to perform MP-PCA tensor denoising[87–89] with Rician bias correction[90], followed by Gibbs ringing correction for partial-Fourier acquisitions[91,92]. Correction for eddy current induced distortions was performed using TOPUP[93] followed by EDDY[94] from FMRIB Software library (FSL, Oxford, UK)[95]. Scalar maps of MTsat were generated from the MT protocol as outlined previously[26]. From the OGSE dMRI data, Mrtrix3 was used to fit the diffusion tensor and acquire maps of MD at each frequency. Diffusion dispersion rate (Λ) maps were computed as outlined in Eq. (3).

For the tensor-valued dMRI data, maps of K_{total} and K_{iso} were generated by jointly fitting:

$$\ln\left(\frac{S_{LTE}}{S_0}\right) = -bD + \frac{b^2D^2K_{total}}{6} \quad (4)$$

$$\ln\left(\frac{S_{STE}}{S_0}\right) = -bD + \frac{b^2D^2K_{iso}}{6} \quad (5)$$

with ordinary least squares, where S_{LTE} and S_{STE} are the diffusion-weighted signal from LTE and STE acquisitions, S_0 is the signal with no diffusion weighting, b is the b-value, and D is the diffusivity[28]. K_{aniso} maps were generated using Eq. (1). MD and FA were computed by performing a diffusional kurtosis fit of the LTE acquisitions from the tensor-valued protocol.

Region-of-interest (ROI) analysis

Quantitative MRI parameters were investigated in three regions of interest: global white matter (WM), the cortex (CX), and the hippocampus (HC). Masks for these three ROIs were generated from the labeled Turone mouse brain atlas[96], which was downsampled to the resolution of the T2-weighted images. To ensure accurate registration of scalar maps to the atlas, a T2 template, an FA template, and an MT-weighted template was created based on images from all scanning sessions using ANTs software[97]. There are three steps to warp individual scalar maps to the down sampled atlas space: (1) Individual FA and MT-weighted maps are registered to their respective templates, (2) the FA and MT templates are registered to the T2 template, and (3) the T2 template is registered to the down sampled atlas. Each registration step involves affine transformation followed by symmetric diffeomorphic transformation using ANTs software. Output deformation fields and affine transforms from each of the three steps were used to warp the individual scalar maps to the atlas space, resulting in only a single interpolation during registration, to obtain quantitative values for each dMRI metric. Voxels in each mask with MD > 0.9 µm^2/ms were excluded to reduce partial volume effects with cerebrospinal fluid.

Statistics and reproducibility

While many studies have shown a quadratic fit of MRI metrics with age, given our reduced age range of 3–8 months we first tested whether our data is better fit by a linear or quadratic model. Model selection testing using the corrected Akaike Information Criterion (AICc)[98] was performed for each MRI metric in our three large ROIs (WM, CX, HC) to test each model. To examine how MRI metrics change over time and possible effects of sex, a multiple linear regression model was performed for each metric in each ROI, to determine effects of age, sex, and age-by-sex interactions. To correct for multiple comparisons, p-values were adjusted using a false discovery rate (FDR) correction via the Benjamini-Hochberg procedure[99], applied separately to model fit, age, sex, and age-by-sex interaction p-values. To examine how MRI metrics change over time in smaller ROIs, we performed the same multiple linear regression and multiple comparison correction used for larger ROIs. Finally, to determine significant differences in histological staining (Olig2, MBP,

GFAP, Iba-1) at 3 vs 8 months of age, a one-tailed Mann-Whitney U test was used within each ROI. Statistical analysis was performed in R version 4.1.2 and GraphPad Prism version 10.2.0.

Reporting summary

Further information on research design is available in the Nature Portfolio Reporting Summary linked to this article.

Data availability

All numerical data values are provided in Supplementary Data 1. All raw and processed MRI imaging data that support the findings of this study are available open-access from The Federated Research Data Repository with identifier https://doi.org/10.20383/103.0594[100], with all data acquisition and processing details available in Rahman et al.[26].

Code availability

All code to process raw data to scalar maps is available in The Federated Research Data Repository, mentioned above. The code is also available publicly through GitLab: https://gitlab.com/cfmm/pipelines/mouse_dmri_MT_dicomTOscalarMaps.

Received: 3 January 2025; Accepted: 30 September 2025;
Published online: 19 November 2025

References

1. Kiely, M. et al. Insights into human cerebral white matter maturation and degeneration across the adult lifespan. *Neuroimage* **247**, 118727 (2022).
2. Bethlehem, R. A. I. et al. Brain charts for the human lifespan. *Nature* **604**, 525–533 (2022).
3. Lebel, C., Walker, L., Leemans, A., Phillips, L. & Beaulieu, C. Microstructural maturation of the human brain from childhood to adulthood. *Neuroimage* **40**, 1044–1055 (2008).
4. Das, S. K., Wang, J. L., Bing, L., Bhetuwal, A. & Yang, H. F. Regional values of diffusional kurtosis estimates in the healthy brain during normal aging. *Clin. Neuroradiol.* **27**, 283–298 (2017).
5. Lätt, J. et al. Regional values of diffusional kurtosis estimates in the healthy brain. *J. Magn. Reson. Imaging* **37**, 610–618 (2013).
6. Korbmacher, M. et al. Brain-wide associations between white matter and age highlight the role of fornix microstructure in brain ageing. *Hum. Brain Mapp.* **44**, 4101–4119 (2023).
7. Le Bihan, D. Looking into the functional architecture of the brain with diffusion MRI. *Nat. Rev. Neurosci.* **4**, 469–480 (2003).
8. Afzali, M. et al. The sensitivity of diffusion MRI to microstructural properties and experimental factors. *J. Neurosci. Methods* **347**, 108951 (2021).
9. Szczepankiewicz, F. et al. The link between diffusion MRI and tumor heterogeneity: Mapping cell eccentricity and density by diffusional variance decomposition (DIVIDE). *Neuroimage* **142**, 522–532 (2016).
10. Jensen, J. H., Helpern, J. A., Ramani, A., Lu, H. & Kaczynski, K. Diffusional kurtosis imaging: the quantification of non-Gaussian water diffusion by means of magnetic resonance imaging. *Magn. Reson Med.* **53**, 1432–1440 (2005).
11. Kamiya, K. et al. Brain White-matter degeneration due to aging and parkinson disease as revealed by double diffusion encoding. *Front. Neurosci.* **14**, 584510 (2020).
12. DEMETRIUS, L. Aging in mouse and human systems. *Ann. N. Y Acad. Sci.* **1067**, 66–82 (2006).
13. Dutta, S. & Sengupta, P. Men and mice: relating their ages. *Life Sci.* **152**, 244–248 (2016).
14. Hammelrath, L. et al. Morphological maturation of the mouse brain: an in vivo MRI and histology investigation. *Neuroimage* **125**, 144–152 (2016).
15. Mengler, L. et al. Brain maturation of the adolescent rat cortex and striatum: changes in volume and myelination. *Neuroimage* **84**, 35–44 (2014).
16. Dvorak, A. V. et al. An atlas for human brain myelin content throughout the adult life span. *Sci. Rep.* **11**, 269 (2021).
17. Slater, D. A. et al. Evolution of white matter tract microstructure across the life span. *Hum. Brain Mapp.* **40**, 2252–2268 (2019).
18. Kim, H. G., Han, D., Kim, J., Choi, J.-S. & Cho, K.-O. 3D MR fingerprinting-derived myelin water fraction characterizing brain development and leukodystrophy. *J. Transl. Med.* **21**, 914 (2023).
19. Beaulieu, C. The basis of anisotropic water diffusion in the nervous system - a technical review. *NMR Biomed.* **15**, 435–455 (2002).
20. Han, X., Geng, Z., Zhu, Q., Song, Z. & Lv, H. Diffusion kurtosis imaging: An efficient tool for evaluating age-related changes in rat brains. *Brain Behav.* **11**, e02136 (2021).
21. Cheung, M. M. et al. Does diffusion kurtosis imaging lead to better neural tissue characterization? A rodent brain maturation study. *Neuroimage* **45**, 386–392 (2009).
22. Reveley, C., Ye, F. Q. & Leopold, D. A. Diffusion kurtosis imaging, MAP-MRI and NODDI selectively track gray matter myelin density in the primate cerebral cortex. *Imaging Neurosci.* **2**, 1–18 (2024).
23. Lema, A. et al. A comparison of magnetization transfer methods to assess brain and cervical cord microstructure in multiple sclerosis. *J. Neuroimaging* **27**, 221–226 (2017).
24. Helms, G., Dathe, H., Kallenberg, K. & Dechent, P. High-resolution maps of magnetization transfer with inherent correction for RF inhomogeneity and *T* 1 relaxation obtained from 3D FLASH MRI. *Magn. Reson Med.* **60**, 1396–1407 (2008).
25. Flurkey, K., Currer, J. & Harrison, D. *The Mouse in Biomedical Research: Normative Biology, Husbandry, and Models*. vol. 3 (Academic Press, 2006).
26. Rahman, N., Xu, K., Budde, M. D., Brown, A. & Baron, C. A. A longitudinal microstructural MRI dataset in healthy C57Bl/6 mice at 9.4 Tesla. *Sci. Data* **10**, 94 (2023).
27. Szczepankiewicz, F., Westin, C.-F. & Nilsson, M. Gradient waveform design for tensor-valued encoding in diffusion MRI. *J. Neurosci. Methods* **348**, 109007 (2021).
28. Arezza, N. J. J., Tse, D. H. Y. & Baron, C. A. Rapid microscopic fractional anisotropy imaging via an optimized linear regression formulation. *Magn. Reson Imaging* **80**, 132–143 (2021).
29. Westin, C.-F. et al. Q-space trajectory imaging for multidimensional diffusion MRI of the human brain. *Neuroimage* **135**, 345–362 (2016).
30. Lasič, S., Szczepankiewicz, F., Eriksson, S., Nilsson, M. & Topgaard, D. Microanisotropy imaging: quantification of microscopic diffusion anisotropy and orientational order parameter by diffusion MRI with magic-angle spinning of the q-vector. *Front. Phys.* **2**, 11 (2014).
31. Schachter, M., Does, M. D., Anderson, A. W. & Gore, J. C. Measurements of restricted diffusion using an oscillating gradient spin-echo sequence. *J. Magn. Reson.* **147**, 232–237 (2000).
32. Does, M. D., Parsons, E. C. & Gore, J. C. Oscillating gradient measurements of water diffusion in normal and globally ischemic rat brain. *Magn. Reson Med.* **49**, 206–215 (2003).
33. Arbabi, A., Kai, J., Khan, A. R. & Baron, C. A. Diffusion dispersion imaging: mapping oscillating gradient spin-echo frequency dependence in the human brain. *Magn. Reson Med* **83**, 2197–2208 (2020).
34. Xu, J., Does, M. D. & Gore, J. C. Quantitative characterization of tissue microstructure with temporal diffusion spectroscopy. *J. Magn. Reson.* **200**, 189–197 (2009).
35. Novikov, D. S., Jensen, J. H., Helpern, J. A. & Fieremans, E. Revealing mesoscopic structural universality with diffusion. *Proc. Natl. Acad. Sci. USA* **111**, 5088–5093 (2014).
36. Baron, C. A. et al. Reduction of diffusion-weighted imaging contrast of acute ischemic stroke at short diffusion times. *Stroke* **46**, 2136–2141 (2015).

37. Lebel, C. & Deoni, S. The development of brain white matter microstructure. *Neuroimage* **182**, 207–218 (2018).
38. Sturrock, R. R. Myelination of the mouse corpus callosum. *Neuropathol. Appl Neurobiol.* **6**, 415–420 (1980).
39. Rivers, L. E. et al. PDGFRA/NG2 glia generate myelinating oligodendrocytes and piriform projection neurons in adult mice. *Nat. Neurosci.* **11**, 1392–1401 (2008).
40. Rahmanzadeh, R. et al. A comparative assessment of myelin-sensitive measures in multiple sclerosis patients and healthy subjects. *Neuroimage Clin.* **36**, 103177 (2022).
41. Duhamel, G. et al. Validating the sensitivity of inhomogeneous magnetization transfer (ihMT) MRI to myelin with fluorescence microscopy. *Neuroimage* **199**, 289–303 (2019).
42. Santini, T. et al. Investigating microstructural changes between in vivo and perfused ex vivo marmoset brains using oscillating gradient and b-tensor encoded diffusion MRI at 9.4 T. *Magn. Reson. Med.* https://doi.org/10.1002/mrm.30298 (2024).
43. He, Y., Aznar, S., Siebner, H. R. & Dyrby, T. B. In vivo tensor-valued diffusion MRI of focal demyelination in white and deep grey matter of rodents. *Neuroimage Clin.* **30**, 102675 (2021).
44. Andersen, K. W. et al. Disentangling white-matter damage from physiological fibre orientation dispersion in multiple sclerosis. *Brain Commun.* **2**, 77 (2020).
45. Szczepankiewicz, F. et al. Quantification of microscopic diffusion anisotropy disentangles effects of orientation dispersion from microstructure: applications in healthy volunteers and in brain tumors. *Neuroimage* **104**, 241–252 (2015).
46. Lee, H.-H., Papaioannou, A., Kim, S.-L., Novikov, D. S. & Fieremans, E. A time-dependent diffusion MRI signature of axon caliber variations and beading. *Commun. Biol.* **3**, 354 (2020).
47. Nilsson, M. et al. Tensor-valued diffusion MRI in under 3 min: an initial survey of microscopic anisotropy and tissue heterogeneity in intracranial tumors. *Magn. Reson Med.* **83**, 608–620 (2020).
48. Nishiyama, A., Shimizu, T., Sherafat, A. & Richardson, W. D. Life-long oligodendrocyte development and plasticity. *Semin Cell Dev. Biol.* **116**, 25–37 (2021).
49. Tripathi, R. B. et al. Remarkable stability of myelinating oligodendrocytes in mice. *Cell Rep.* **21**, 316–323 (2017).
50. Genc, S. et al. MRI signatures of cortical microstructure in human development align with oligodendrocyte cell-type expression. *Nat. Commun.* **16**, 3317 (2025).
51. Askew, K. et al. Coupled proliferation and apoptosis maintain the rapid turnover of microglia in the adult brain. *Cell Rep.* **18**, 391–405 (2017).
52. Long, J. M. et al. Stereological analysis of astrocyte and microglia in aging mouse hippocampus. *Neurobiol. Aging* **19**, 497–503 (1998).
53. Bondi, H., Bortolotto, V., Canonico, P. L. & Grilli, M. Complex and regional-specific changes in the morphological complexity of GFAP+ astrocytes in middle-aged mice. *Neurobiol. Aging* **100**, 59–71 (2021).
54. Walker, D. G. & Lue, L.-F. Immune phenotypes of microglia in human neurodegenerative disease: challenges to detecting microglial polarization in human brains. *Alzheimers Res. Ther.* **7**, 56 (2015).
55. Wilhelmsson, U. et al. Redefining the concept of reactive astrocytes as cells that remain within their unique domains upon reaction to injury. *Proc. Natl. Acad. Sci. USA* **103**, 17513–17518 (2006).
56. Valério-Gomes, B., Guimarães, D. M., Szczupak, D. & Lent, R. The absolute number of oligodendrocytes in the adult mouse brain. *Front. Neuroanat.* **12**, 90 (2018).
57. Hilscher, M. M. et al. Spatial and temporal heterogeneity in the lineage progression of fine oligodendrocyte subtypes. *BMC Biol.* **20**, 122 (2022).
58. Sepehrband, F. et al. Perivascular space fluid contributes to diffusion tensor imaging changes in white matter. *Neuroimage* **197**, 243–254 (2019).
59. Lynch, K. M., Sepehrband, F., Toga, A. W. & Choupan, J. Brain perivascular space imaging across the human lifespan. *Neuroimage* **271**, 120009 (2023).
60. Cox, S. R. et al. Ageing and brain white matter structure in 3513 UK Biobank participants. *Nat. Commun.* **7**, 13629 (2016).
61. Chen, J., Bayanagari, V. L., Chung, S., Wang, Y. & Lui, Y. W. Deep learning with diffusion MRI as in vivo microscope reveals sex-related differences in human white matter microstructure. *Sci. Rep.* **14**, 9835 (2024).
62. Lawrence, K. E. et al. Age and sex effects on advanced white matter microstructure measures in 15,628 older adults: a UK biobank study. *Brain Imaging Behav.* **15**, 2813–2823 (2021).
63. Kaczkurkin, A. N., Raznahan, A. & Satterthwaite, T. D. Sex differences in the developing brain: insights from multimodal neuroimaging. *Neuropsychopharmacology* **44**, 71–85 (2019).
64. Zhou, M. et al. Tensor-valued diffusion MRI of human acute stroke. *Magn. Reson. Med.* **91**, 2126–2141 (2024).
65. Song, H. et al. Sex differences in the extent of acute axonal pathologies after experimental concussion. *Acta Neuropathol.* **147**, 79 (2024).
66. Jespersen, S. N., Olesen, J. L., Ianuş, A. & Shemesh, N. Effects of nongaussian diffusion on "isotropic diffusion" measurements: an ex-vivo microimaging and simulation study. *J. Magn. Reson.* **300**, 84–94 (2019).
67. Novello, L. et al. In vivo correlation tensor MRI reveals microscopic kurtosis in the human brain on a clinical 3T scanner. *Neuroimage* **254**, 119137 (2022).
68. Henriques, R. N., Jespersen, S. N. & Shemesh, N. Evidence for microscopic kurtosis in neural tissue revealed by correlation tensor MRI. *Magn. Reson. Med.* **86**, 3111–3130 (2021).
69. Alves, R. et al. Correlation tensor MRI deciphers underlying kurtosis sources in stroke. *Neuroimage* **247**, 118833 (2022).
70. Martínez-Tazo, P., Santos, A., Selim, M. K., Espinós-Soler, E. & De Santis, S. Sex matters: the MouseX DW-ALLEN Atlas for mice diffusion-weighted MR imaging. *Neuroimage* **292**, 120573 (2024).
71. Bergles, D. E. & Richardson, W. D. Oligodendrocyte development and plasticity. *Cold Spring Harb. Perspect. Biol.* **8**, a020453 (2016).
72. Fu, Y., Rusznák, Z., Herculano-Houzel, S., Watson, C. & Paxinos, G. Cellular composition characterizing postnatal development and maturation of the mouse brain and spinal cord. *Brain Struct. Funct.* **218**, 1337–1354 (2013).
73. Olesen, J. L., Østergaard, L., Shemesh, N. & Jespersen, S. N. Diffusion time dependence, power-law scaling, and exchange in gray matter. *Neuroimage* **251**, 118976 (2022).
74. Jelescu, I. O., de Skowronski, A., Geffroy, F., Palombo, M. & Novikov, D. S. Neurite Exchange Imaging (NEXI): a minimal model of diffusion in gray matter with inter-compartment water exchange. *Neuroimage* **256**, 119277 (2022).
75. Novikov, D. S., Kiselev, V. G. & Jespersen, S. N. On modeling. *Magn. Reson. Med.* **79**, 3172–3193 (2018).
76. Jelescu, I. O., Palombo, M., Bagnato, F. & Schilling, K. G. Challenges for biophysical modeling of microstructure. *J. Neurosci. Methods* **344**, 108861 (2020).
77. Palombo, M. et al. SANDI: a compartment-based model for non-invasive apparent soma and neurite imaging by diffusion MRI. *Neuroimage* **215**, 116835 (2020).
78. Rahman, N., Ramnarine, J., Xu, K., Brown, A. & Baron, C. A. Test–retest reproducibility of in vivo magnetization transfer ratio and saturation index in mice at 9.4 Tesla. *J. Magn. Reson. Imaging* **56**, 893–903 (2022).
79. Rahman, N. et al. Test-retest reproducibility of in vivo oscillating gradient and microscopic anisotropy diffusion MRI in mice at 9.4 Tesla. *PLoS One* **16**, e0255711 (2021).

80. Vutskits, L. & Xie, Z. Lasting impact of general anaesthesia on the brain: mechanisms and relevance. *Nat. Rev. Neurosci.* **17**, 705–717 (2016).
81. Hamilton, J. et al. Robust frequency-dependent diffusional kurtosis computation using an efficient direction scheme, axisymmetric modelling, and spatial regularization. *Imaging Neurosci.* **2**, 1–22 (2024).
82. Borsos, K. B., Tse, D. H. Y., Dubovan, P. I. & Baron, C. A. Tuned bipolar oscillating gradients for mapping frequency dispersion of diffusion kurtosis in the human brain. *Magn. Reson. Med.* **89**, 756–766 (2023).
83. Haber, M. et al. Defining an analytic framework to evaluate quantitative MRI markers of traumatic axonal injury: preliminary results in a mouse closed head injury model. *eNeuro* **4**, ENEURO.0164-17.2017 (2017).
84. Schindelin, J. et al. Fiji: an open-source platform for biological-image analysis. *Nat. Methods* **9**, 676–682 (2012).
85. Vos, S. B. et al. The importance of correcting for signal drift in diffusion MRI. *Magn. Reson. Med.* **77**, 285–299 (2017).
86. Chen, J. et al. Optimization and validation of the DESIGNER preprocessing pipeline for clinical diffusion MRI in white matter aging. *Imaging Neurosci.* **2**, 1–17 (2024).
87. Olesen, J. L., Ianus, A., Østergaard, L., Shemesh, N. & Jespersen, S. N. Tensor denoising of multidimensional MRI data. *Magn. Reson Med* **89**, 1160–1172 (2023).
88. Gavish, M. & Donoho, D. L. Optimal shrinkage of singular values. *IEEE Trans. Inf. Theory* **63**, 2137–2152 (2017).
89. Veraart, J. et al. Denoising of diffusion MRI using random matrix theory. *Neuroimage* **142**, 394–406 (2016).
90. Koay, C. G. & Basser, P. J. Analytically exact correction scheme for signal extraction from noisy magnitude MR signals. *J. Magn. Reson.* **179**, 317–322 (2006).
91. Kellner, E., Dhital, B., Kiselev, V. G. & Reisert, M. Gibbs-ringing artifact removal based on local subvoxel-shifts. *Magn. Reson. Med* **76**, 1574–1581 (2016).
92. Lee, H., Novikov, D. S. & Fieremans, E. Removal of partial Fourier-induced Gibbs (RPG) ringing artifacts in MRI. *Magn. Reson Med.* **86**, 2733–2750 (2021).
93. Andersson, J. L. R., Skare, S. & Ashburner, J. How to correct susceptibility distortions in spin-echo echo-planar images: application to diffusion tensor imaging. *Neuroimage* **20**, 870–888 (2003).
94. Andersson, J. L. R. & Sotiropoulos, S. N. An integrated approach to correction for off-resonance effects and subject movement in diffusion MR imaging. *Neuroimage* **125**, 1063–1078 (2016).
95. Smith, S. M. et al. Advances in functional and structural MR image analysis and implementation as FSL. *Neuroimage* **23**, S208–S219 (2004).
96. Barrière, D. A. et al. Brain orchestration of pregnancy and maternal behavior in mice: a longitudinal morphometric study. *Neuroimage* **230**, 117776 (2021).
97. Avants, B. B. et al. A reproducible evaluation of ANTs similarity metric performance in brain image registration. *Neuroimage* **54**, 2033–2044 (2011).
98. Akaike, H. A new look at the statistical model identification. *IEEE Trans. Autom. Contr* **19**, 716–723 (1974).
99. Benjamini, Y., Heller, R. & Yekutieli, D. Selective inference in complex research. *Philos. Trans. R. Soc. A: Math., Phys. Eng. Sci.* **367**, 4255–4271 (2009).
100. Rahman, N., Xu, K., Budde, M., Brown, A. & Baron, C. A longitudinal microstructural MRI dataset in healthy C57Bl/6 mice at 9.4 Tesla. *Federated Research Data Repository* (FDA, 2022).

Acknowledgements

This work was supported by the New Frontiers in Research Fund – Exploration grant #NFRFE-2018-01290, Canada Research Chair Program #950-231993, the Canada First Research Excellence Fund (BrainsCAN), the Natural Sciences and Engineering Research Council of Canada – Canada Graduate Scholarships – Doctoral (NSERC CGSD) program, and partially supported by the National Hockey League Players Association Challenge Fund. The authors thank Alex Li and Miranda Bellyou for their support in data acquisition and animal handling.

Author contributions

N.R. contributed to Conceptualization, Data curation, Formal analysis, Investigation, Visualization, Writing – original draft, Writing – review & editing; J.H. contributed to Conceptualization, Formal analysis, Investigation, Visualization, Writing – original draft, Writing – review & editing; K.X. contributed to Project administration, Resources, Writing – review & editing; A.B. contributed to Funding acquisition, Project administration, Resources, Supervision, Writing – review & editing; C.A.B. contributed to Conceptualization, Funding acquisition, Resources, Supervision, Writing – review & editing.

Competing interests

The authors declare no competing interests.

Additional information

Supplementary information The online version contains supplementary material available at https://doi.org/10.1038/s42003-025-08981-1.

Correspondence and requests for materials should be addressed to Corey A. Baron.

Peer review information *Communications Biology* thanks Ileana Jelescu, Jong-Hyun Bae and the other, anonymous, reviewer(s) for their contribution to the peer review of this work. Primary Handling Editor: Benjamin Bessieres.

Reprints and permissions information is available at http://www.nature.com/reprints

Publisher's note Springer Nature remains neutral with regard to jurisdictional claims in published maps and institutional affiliations.

Open Access This article is licensed under a Creative Commons Attribution-NonCommercial-NoDerivatives 4.0 International License, which permits any non-commercial use, sharing, distribution and reproduction in any medium or format, as long as you give appropriate credit to the original author(s) and the source, provide a link to the Creative Commons licence, and indicate if you modified the licensed material. You do not have permission under this licence to share adapted material derived from this article or parts of it. The images or other third party material in this article are included in the article's Creative Commons licence, unless indicated otherwise in a credit line to the material. If material is not included in the article's Creative Commons licence and your intended use is not permitted by statutory regulation or exceeds the permitted use, you will need to obtain permission directly from the copyright holder. To view a copy of this licence, visit http://creativecommons.org/licenses/by-nc-nd/4.0/.

© The Author(s) 2025